European Transport \ Trasporti Europei (2019) Issue 71, Paper n° 5, ISSN 1825-3997

Modelling and vehicle based measurements of ballast settlements under the common crossing

Mykola Sysyn[1*], Ulf Gerber[1], Dimitri Gruen[1], Olga Nabochenko[2], Vitalii Kovalchuk[2]

[1]*Institute of Railway Systems and Public Transport, Technical University of Dresden, Dresden, Germany;*
[2]*Department of the rolling stock and track, Lviv branch of Dnipropetrovsk National University of Railway Transport, Lviv, Ukraine*

Abstract

Railway turnout is geometrically and physically inhomogeneous object of railway superstructure. The common crossing zone is the high-loaded part of turnout with relatively short lifecycle. The different degradation processes are taking place in the common crossing. On the one hand, the frog nose and wingrail are wearing with inhomogeneous intensity, on the other hand the ballast under the crossing zone is uniformly deformed that lead to appearing the void wave along the crossing axis. The two deterioration processes are interconnected and both influence the dynamic loading. The paper deals with research of both influences based on the mathematical modelling and simulation together with the analysis of inertial vehicle based measurements. The ballast settlements behavior is simulated with the numerical model and compared with the settlements measured with axle-box accelerations system. The current research makes the base for the following inertial diagnostic vehicle and track based investigations as well as planning the maintenance works at common crossing.

Keywords: railway turnout, common crossing, ballast settlements, track stiffness, inertial measurements, vehicle based measurements.

1. Introduction

At present, the diagnostics of turnout's common crossing is usually implemented with visual inspection and geometry measurements of frog nose and wing rail. Many authors (Gerber, Zoll and Fengler, 2013) point out those such inspection methods cannot provide the plausible estimation of crossing state and reliably predict the lifetime of crossing rails. The fact is demonstrated by Gerber, Zoll and Fengler (2015) with quite different fatigue lifetime of rolling surface, from 25 to 160 megatons, with similar wear, material and the evidentially the same operational conditions of "DB System technik" test line. Moreover, the diagnostics of ballast state with the geometry measurement without preloading is quite impossible. However, the ballast layer state plays an

[*] Corresponding author: Mykola Sysyn (mykola.sysyn@tu-dresden.de)

important role in formation of common crossing dynamic loading and the following initiation and growth of rolling surface fatigue defects. The influence mechanism can be depicted with the following scheme (*Figure 1*). The degradation process of rolling surface depends not only on geometrical irregularity and wear, but also on the track stiffness that depends on sleeper voids and inhomogeneous ballast settlements.

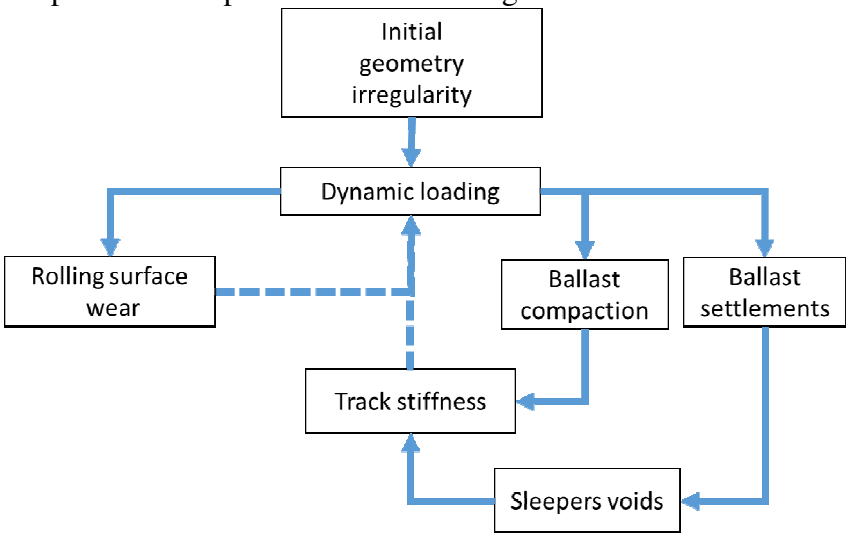

Figure1: Interrelation of rolling surface and ballast degradation processes

To provide the objective estimation of common crossings, the inertial measurement systems were developed with German Railway Company (Zoll, Gerber and Fengler,2016). Such systems are based on vehicle acceleration measurements with system of ESAH-F (Electronic Analysis System of Crossing – Train) (*Figure 2, left*) and on track acceleration measurements with system of ESAH-M (Electronic Analysis System of Crossing – Portable) (*Figure 2, right*). Those systems consist of one 3-D acceleration sensors together with the positioning sensors.

Figure 2: The inertial measurement systems ESAH-F (left) and ESAH-M (right)
Source: http://witt-solutions.de , http://www.bahnbilder.de/

The present paper deals with the modelling and vehicle based measurements of ballast settlements under the common crossing. The main goal of the research is the development of methods for prediction of switch geometry degradation due to

inhomogenous ballast settlements. The methods are basedon vehicle based measurements diagnostic system ESAH-F.

The modeling of the deformation in the crossing area is divided into two subareas: short-term modeling and long-term modeling. The short-term modeling is related to the quick temporal and spatial dependent deformation in the crossing area under the action of a moving wheel. This deformation is dependent on the one hand on track geometry deviation and on the other hand on the distribution of masses and stiffness in the track.

The long-term modeling is related to the slow temporal and local dependent change of the track position change, which in turn is coupled back to the ballast settlement in the crossing area via a change in the ballast stiffness. Absolute quantity for the "long-term" is the number of load cycles, which can be converted at any time with knowledge of the annually accumulated load alternation in a "long-term" (usually in the dimension months or years). Finally, by coupling the short-term and long-term modeling, the short-term behavior, i.e. the measurable deformation in the crossing section, can be determined as a function of the number of load cycles.

Many recent studies are concentrated on improvement of railway track and turnout condition monitoring (Sysyn et al., 2019a; Kovalchuk et al., 2018b; Uhl, Mendrok and Chudzikiewicz, 2010). The performance of inertial monitoring method for railway turnouts is studied in (Sysyn, Kovalchuk and Jiang,2018). The improvement of longitudinal profile of frogs at railroad switches with aim of their lifecycle prolongation is carried out in (Kovalchuket al., 2018c).

The problem of track geometry deterioration due to ballast settlements is picked out as a central theme by many authors. The long-term ballast settlements in transition zones have been studied in (Wang and Markine, 2018; Izvolt, Harusinec and Smalo, 2018). Influence of under sleeper pads in switches & crossings on track settlements is considered in (Plášek and Hruzíková, 2017).

The interaction of track irregularity and long-term settlements in transition zone of backfill soil metallic structures was studied in (Kovalchuk et al., 2018a;Izvolt and Kardos, 2011). Authors (Fischer,2017;Németh and Fischer, 2018) studied the influence of dynamic loading on a particle breakage of railway ballast.

The laboratory investigation and numerical modelling of voided sleeper behavior was carried out by Augustin et al.(2003). Holtzendorff (2003) studied the influence of voided sleeper at long-term behavior of railway track geometry in combination with other factors.Plášeket al. (2015) studied the ballast settlements development of switch in the in-situ investigations. The research of the deterioration process due to inhomogeneous ballast settlements is presented in paper of Nagy (2017). The influence of track stiffness as well as many other parameters on inhomogeneous track settlements is considered in (Sysynet al., 2018). Estimation of railway ballast consolidation with inertial measurements is proposed in (Sysyn et al., 2019b). The iterative mathematical modelling of short-time dynamic interaction and long-term settlements process in ordinary railway track is presented in (Nabochenko et al., 2019). The track stiffness change, due to voids is taken into account in the study

The papers of authors (Xin et al., 2014) are devoted to the numerical prediction of track settlement in railway turnout based on complicated 3D FEM and vehicle dynamics modelling with an iterative update of accumulated track settlements. However, the change of track stiffness due to emergence of sleeper voids together with growing ballast stiffness is not taken into account.

2. Short-term modelling

The *Figure 3*shows the model. The vehicle could be reduced to the unsprung mass m_U (wheel).The track is reduced to a beam with the meter mass $\bar{m}_T(x)$ (rail) and the bending stiffness (flexural rail stiffness), which is bedded on a viscoelastic underlay with the meter stiffness $\bar{k}_T(x)$ (total stiffness of bearer, ballast and subsoil) and the meter viscosity $\bar{\eta}_T(x)$ (summary viscosity of bearer, ballast and subsoil).The wheel and rail have immediate coupling between. The geometric shape on the top of rail (track geometry error) $z_E(x)$ acts as a dynamic excitation of the vibration system vehicle - track. The vehicle applies a quasistatic loading $F_0(t)$ to the track and moves at constant speed v along the way x. The loading corresponds to the static weight and dynamic part due to sprung weight oscillation reduced to one wheel. It is assumed, for simplicity reasons that the sprung weight oscillation have own frequency 1-2 Hz and are calculated with one mass-spring relation depending on the wheel trajectory. The assumed own frequency corresponds to the car suspension of trains for the line where system ESAH-F was used and agrees to that of literature sources (Esveld, 2001;Popp et al., 2005).

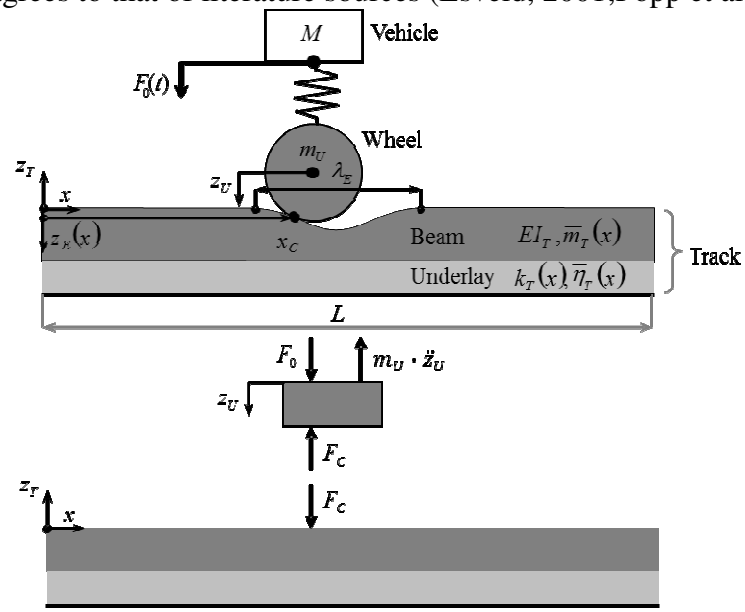

Figure 3: Dynamic model

2.2 Calculation algorithm

By free cutting the entire system, there are two subsystems: the track in the form of the viscoelastically embedded beam and the vehicle as a single mass. The contact force F_C acts between both subsystems (*Figure 3*). Initially both subsystems are to consider separately. The differential equation of the viscoelastic embedded beam consists of 5 terms: the mass inertiaterm $\bar{m}_T \cdot \ddot{z}_T$ proportional to the (vertical) acceleration $\ddot{z}_T$, the viscous term $\bar{\eta}_T \cdot \dot{z}_T$ proportional to the (vertical) velocity $\dot{z}_T$, the elastic term $\bar{k}_T \cdot z_T$ proportional to the (vertical) displacement z_T,the bending term $EI_T \cdot z_T''''$ proportional to

the quadruple local derivative $\mathbf{z}_T''''$, and the excitation term $\boldsymbol{q}_E$. According to *Figure 3*this is:

$$-\bar{\boldsymbol{m}}_T \cdot \ddot{\mathbf{z}}_T - \bar{\eta}_T \cdot \dot{\mathbf{z}}_T - \bar{\boldsymbol{k}}_T \cdot \mathbf{z}_T - \boldsymbol{EI}_T \cdot \mathbf{z}_T'''' = \boldsymbol{q}_E \tag{1}$$

Equation (1) is a partial differential equation, which contains its temporal and spatial derivatives in addition to the displacement $\mathbf{z}_T$:

$$\dot{\mathbf{z}}_T = \frac{\partial \mathbf{z}_T}{\partial \mathbf{t}},\ \ddot{\mathbf{z}}_T = \frac{\partial^2 \mathbf{z}_T}{\partial \mathbf{t}^2},\ \mathbf{z}_T'''' = \frac{\partial^4 \mathbf{z}_T}{\partial \mathbf{x}^4} \tag{2}$$

The solution of (1)is numeric. For this, the local differential quotient $\mathbf{z}_T''''$ is converted first into a local difference quotient (with the introduction of a local discretization with the increment $\Delta \boldsymbol{x}$):

$$\mathbf{z}_T'''' \rightarrow \frac{\mathbf{z}_{T,j+2} - 4 \cdot \mathbf{z}_{T,j+1} + 6 \cdot \mathbf{z}_{T,j} - 4 \cdot \mathbf{z}_{T,j-1} + \mathbf{z}_{T,j-2}}{\left(\Delta \boldsymbol{x}\right)^4} \tag{3}$$

The transition to the difference quotient corresponds to the decomposition of the continuous beam of length $\boldsymbol{L}$ into $\boldsymbol{j} = 1 \ldots \boldsymbol{n}_x$ beam elements of length $\Delta \boldsymbol{x}$. The number of beam elements results to:

$$\boldsymbol{n}_x = \frac{\boldsymbol{L}}{\Delta \boldsymbol{x}} \tag{4}$$

The excitation load $\boldsymbol{q}_E$ (line load) is expressed as a function of the contact force $\boldsymbol{F}_C$ by converting the contact force into a constant line load over the length $\Delta \boldsymbol{x}$ of the beam element:

$$\boldsymbol{q}_E = \delta \cdot \frac{\boldsymbol{F}_C}{\Delta \boldsymbol{x}} \tag{5}$$

The introduction of the operation vector $\boldsymbol{\delta}$ of the dimension $\boldsymbol{n}_x$ results from the fact that only the beam element located at the contact point $\boldsymbol{x}_C$ is loaded. The location of the contact point is:

$$\boldsymbol{x}_C = \boldsymbol{x}_0 + \boldsymbol{v} \cdot \boldsymbol{t} \tag{6}$$

Here, the wheel is placed on the locus $\boldsymbol{x}_0$ at the time $\boldsymbol{t}_0$.

The elements of the operation vector $\boldsymbol{\delta}_j$ can only assume the two states one or zero, depending on whether or not the contact force acts on the concerned beam element:

$$\begin{aligned} \boldsymbol{\delta}_j &= 1 \ \text{ for } \ \boldsymbol{j} \cdot \Delta \boldsymbol{x} = \boldsymbol{x}_C \\ \boldsymbol{\delta}_j &= 0 \ \text{ for } \ \boldsymbol{j} \cdot \Delta \boldsymbol{x} \neq \boldsymbol{x}_C \end{aligned} \tag{7}$$

Substituting (3) and (5) into (1) yields a difference equation for a single beam element of length Δx :

$$-\bar{m}_{T,j} \cdot \ddot{z}_{T,j} - \bar{\eta}_{T,j} \cdot \dot{z}_{T,j} - \bar{k}_{T,j} \cdot z_{T,j} - \frac{EI_T}{(\Delta x)^4} \cdot \begin{pmatrix} 1 \cdot z_{T,j-2} \\ -4 \cdot z_{T,j-1} \\ 6 \cdot z_{T,j} \\ -4 \cdot z_{T,j+1} \\ 1 \cdot z_{T,j+2} \end{pmatrix} = \frac{\delta_j}{\Delta x} \cdot F_C \tag{8}$$

or after conversion:

$$-\bar{m}_{T,j} \cdot \ddot{z}_{T,j} - \bar{\eta}_{T,j} \cdot \dot{z}_{T,j} - \begin{pmatrix} \frac{1 \cdot EI_T}{(\Delta x)^4} \\ \frac{-4 \cdot EI_T}{(\Delta x)^4} \\ \frac{6 \cdot EI_T}{(\Delta x)^4} + \bar{k}_{T,j} \\ \frac{-4 \cdot EI_T}{(\Delta x)^4} \\ \frac{1 \cdot EI_T}{(\Delta x)^4} \end{pmatrix} \cdot \begin{pmatrix} z_{T,j-2} \\ z_{T,j-1} \\ z_{T,j} \\ z_{T,j+1} \\ z_{T,j+2} \end{pmatrix} = \frac{\delta_j}{\Delta x} \cdot F_C \tag{9}$$

The combination of beam elements to the total beam of length L results in an equation system of degree n_x , which assumes the following appearance in matrix notation:

$$-\mathbf{M}_T \cdot \ddot{\mathbf{z}}_T - \mathbf{H}_T \cdot \dot{\mathbf{z}}_T - K_T \cdot \mathbf{z}_T = X \tag{10}$$

The mass matrix $\mathbf{M}_T$ of size $n_x \times n_x$ is composed of the meter masses of the beam elements $\bar{m}_{T,j}$:

$$\mathbf{M}_T = \begin{bmatrix} \bar{m}_{T,1} & 0 & 0 & 0 & 0 \\ 0 & \bar{m}_{T,2} & 0 & 0 & 0 \\ 0 & 0 & \ddots & 0 & 0 \\ 0 & 0 & 0 & \bar{m}_{T,n_x-1} & 0 \\ 0 & 0 & 0 & 0 & \bar{m}_{T,n_x} \end{bmatrix} \tag{11}$$

The damping matrix $\mathbf{H}_T$ of dimension $n_x \times n_x$ is composed of the meter viscosities of the beam elements $\bar{\eta}_{T,j}$:

$$\mathbf{H}_T = \begin{bmatrix} \overline{\eta}_{T,1} & 0 & 0 & 0 & 0 \\ 0 & \overline{\eta}_{T,2} & 0 & 0 & 0 \\ 0 & 0 & \ddots & 0 & 0 \\ 0 & 0 & 0 & \overline{\eta}_{T,n_x-1} & 0 \\ 0 & 0 & 0 & 0 & \overline{\eta}_{T,n_x} \end{bmatrix} \tag{12}$$

The stiffness matrix $\boldsymbol{K}_T$ of size $\boldsymbol{n}_x \times \boldsymbol{n}_x$ is composed of the meter stiffnesses of the beam elements $\overline{\boldsymbol{k}}_{T,j}$ as well as the bending stiffness of the beam elements $\boldsymbol{EI}_T$:

$$\boldsymbol{K}_T = \begin{bmatrix} \frac{6\cdot \boldsymbol{EI}_T}{(\Delta x)^4} + \overline{\boldsymbol{k}}_{T,1} & \frac{-4\cdot \boldsymbol{EI}_T}{(\Delta x)^4} & \frac{1\cdot \boldsymbol{EI}_T}{(\Delta x)^4} & 0 & 0 \\ \frac{-4\cdot \boldsymbol{EI}_T}{(\Delta x)^4} & \frac{6\cdot \boldsymbol{EI}_T}{(\Delta x)^4} + \overline{\boldsymbol{k}}_{T,2} & \frac{-4\cdot \boldsymbol{EI}_T}{(\Delta x)^4} & \frac{1\cdot \boldsymbol{EI}_T}{(\Delta x)^4} & 0 \\ \ddots & \ddots & \ddots & \ddots & \ddots \\ 0 & \frac{1\cdot \boldsymbol{EI}_T}{(\Delta x)^4} & \frac{-4\cdot \boldsymbol{EI}_T}{(\Delta x)^4} & \frac{6\cdot \boldsymbol{EI}_T}{(\Delta x)^4} + \overline{\boldsymbol{k}}_{T,n_x-1} & \frac{-4\cdot \boldsymbol{EI}_T}{(\Delta x)^4} \\ 0 & 0 & \frac{1\cdot \boldsymbol{EI}_T}{(\Delta x)^4} & \frac{-4\cdot \boldsymbol{EI}_T}{(\Delta x)^4} & \frac{6\cdot \boldsymbol{EI}_T}{(\Delta x)^4} + \overline{\boldsymbol{k}}_{T,n_x} \end{bmatrix} \tag{13}$$

The excitation vector $\boldsymbol{X}$ of the dimension $\boldsymbol{n}_x$ is composed of the contact force $\boldsymbol{F}_C$ and the operation vector $\boldsymbol{\delta}$:

$$\boldsymbol{X} = \frac{\boldsymbol{F}_C}{\Delta x} \cdot \begin{bmatrix} \boldsymbol{\delta}_1 \\ \boldsymbol{\delta}_2 \\ \vdots \\ \boldsymbol{\delta}_{n_x-1} \\ \boldsymbol{\delta}_{n_x} \end{bmatrix} \tag{14}$$

Formula (10)describes the deformation state of the beam (i.e. the rail) in its temporal dependence. Here, three vectors of dimension $\boldsymbol{n}_x$ characterize the deformation state: the displacement vector $\mathbf{z}_T$, the velocity vector $\dot{\mathbf{z}}_T$ and the acceleration vector $\ddot{\mathbf{z}}_T$.
The differential equation of the wheel (i.e. the vehicle) is according to *Figure 3* (below):

$$\boldsymbol{m}_U \cdot \ddot{\mathbf{z}}_U = -\boldsymbol{F}_C \tag{15}$$

From the forced coupling at the contact-point (index $\boldsymbol{C}$) between wheel and rail according to *Figure 3* (above) follows:

$$\mathbf{z}_{ED} = \mathbf{z}_U + \mathbf{z}_{TD} \text{ or } \ddot{\mathbf{z}}_{ED} = \ddot{\mathbf{z}}_U + \ddot{\mathbf{z}}_{TD} \tag{16}$$

Thus, the vertical movement of the vehicle at contact point can be expressed as a function of the vertical track movement and the vertical track geometry error:

$$\ddot{\mathbf{z}}_U = \ddot{\mathbf{z}}_{ED} - \ddot{\mathbf{z}}_{TD} \tag{17}$$

From(15)and(17) follows for the contact force:

$$\boldsymbol{F_C} = -\boldsymbol{m}_U \cdot \left(\ddot{\mathbf{z}}_{ED} - \ddot{\mathbf{z}}_{TD} \right) \tag{18}$$

The movement of the track $\mathbf{z}_{TD}, \dot{\mathbf{z}}_{TD}, \ddot{\mathbf{z}}_{TD}$ and the track geometry error $\mathbf{z}_{ED}, \dot{\mathbf{z}}_{ED}, \ddot{\mathbf{z}}_{ED}$ at the contact point using the operation vector $\boldsymbol{\delta}$ are equal to:

$$\begin{gathered} \mathbf{z}_{TD} = \boldsymbol{\delta} \cdot \mathbf{z}_T \,,\ \dot{\mathbf{z}}_{TD} = \boldsymbol{\delta} \cdot \dot{\mathbf{z}}_T \,,\ \ddot{\mathbf{z}}_{TD} = \boldsymbol{\delta} \cdot \ddot{\mathbf{z}}_T \\ \mathbf{z}_{TD} = \boldsymbol{\delta} \cdot \mathbf{z}_E \,,\ \dot{\mathbf{z}}_{TD} = \boldsymbol{\delta} \cdot \dot{\mathbf{z}}_E \,,\ \ddot{\mathbf{z}}_{TD} = \boldsymbol{\delta} \cdot \ddot{\mathbf{z}}_E \end{gathered} \tag{19}$$

The displacement vectors, velocity and acceleration of the track geometry error $\mathbf{z}_E, \dot{\mathbf{z}}_E, \ddot{\mathbf{z}}_E$ with degree $\boldsymbol{n_x}$ are known. The following applies:

$$\dot{\mathbf{z}}_{E,j} = \boldsymbol{v}^2 \cdot \frac{\mathbf{z}_{E,j+1} + \mathbf{z}_{E,j-1}}{2 \cdot \Delta \boldsymbol{x}} \,,\ \ddot{\mathbf{z}}_{E,j} = \boldsymbol{v}^2 \cdot \frac{\mathbf{z}_{E,j+1} - 2 \cdot \mathbf{z}_{E,j+1} + \mathbf{z}_{E,j-1}}{\left(\Delta \boldsymbol{x} \right)^2} \tag{20}$$

Considering (19), the contact force (18) can be formulated in the following form:

$$\boldsymbol{F_C} = \frac{\boldsymbol{m}_U}{\Delta \boldsymbol{x}} \cdot \left(\boldsymbol{\delta} \cdot \ddot{\mathbf{z}}_E - \boldsymbol{\delta} \cdot \ddot{\mathbf{z}}_T \right) \tag{21}$$

By substituting the contact force $\boldsymbol{F_C}$ in (14), the equation system (10) takes the following form:

$$\mathbf{M}_T \cdot \ddot{\mathbf{z}}_T + \mathbf{H}_T \cdot \dot{\mathbf{z}}_T + \boldsymbol{K}_T \cdot \mathbf{z}_T = \left[\frac{\boldsymbol{m}_U}{\Delta \boldsymbol{x}} \cdot \left(\boldsymbol{\delta} \cdot \ddot{\mathbf{z}}_E - \boldsymbol{\delta} \cdot \ddot{\mathbf{z}}_T \right) \right] \cdot \boldsymbol{\delta} \tag{22}$$

In this case, terms with $\ddot{\mathbf{z}}_T$ appear on both sides of the equation system (22). These are now summarised on the left side of the equation system. The result in a simplified form shows formula(23):

$$\mathbf{M}_{TM} \cdot \ddot{\mathbf{z}}_T + \mathbf{H}_T \cdot \dot{\mathbf{z}}_T + \boldsymbol{K}_T \cdot \mathbf{z}_T = \left[\frac{\boldsymbol{m}_U}{\Delta \boldsymbol{x}} \cdot \boldsymbol{\delta} \cdot \ddot{\mathbf{z}}_E \right] \cdot \boldsymbol{\delta} \tag{23}$$

Here occurs the modified mass matrix $\mathbf{M}_{TM}$, which additionally contains the wheel mass $\boldsymbol{m}_U$:

$$\mathbf{M}_{TM} = \begin{bmatrix} \bar{m}_{T,1} + \delta_1 \cdot \frac{m_U}{\Delta x} & 0 & 0 & 0 & 0 \\ 0 & \bar{m}_{T,2} + \delta_2 \cdot \frac{m_U}{\Delta x} & 0 & 0 & 0 \\ 0 & 0 & \ddots & 0 & 0 \\ 0 & 0 & 0 & \bar{m}_{T,n_x-1} + \delta_{n_x-1} \cdot \frac{m_U}{\Delta x} & 0 \\ 0 & 0 & 0 & 0 & \bar{m}_{T,n_x} + \delta_{n_x} \cdot \frac{m_U}{\Delta x} \end{bmatrix} \tag{24}$$

The equation system (23) calculates the state of deformation of the entire system $(\mathbf{z}_T, \dot{\mathbf{z}}_T, \ddot{\mathbf{z}}_T)$ at the time t .

Next search ingaim is the movement of the whole system, i.e. the temporal change of the deformation state. For this purpose, we calculate the deformation state in k discreet time steps with the time increment Δt , i.e. the temporal differential quotients replaced by temporal difference quotients. Then, the difference quotient for the displacement is:

$$\mathbf{z}_{T,k+1} = \mathbf{z}_{T,k} + \frac{\Delta t}{2} \cdot \left(\dot{\mathbf{z}}_{T,k} + \dot{\mathbf{z}}_{T,k+1} \right) \tag{25}$$

The difference quotient for the velocity is:

$$\dot{\mathbf{z}}_{T,k+1} = \dot{\mathbf{z}}_{T,k} + \frac{\Delta t}{2} \cdot \left(\ddot{\mathbf{z}}_{T,k} + \ddot{\mathbf{z}}_{T,k+1} \right) \tag{26}$$

The combination of (24)and(25) results in the difference quotient for the acceleration:

$$\ddot{\mathbf{z}}_{T,k+1} = \frac{4}{\Delta t^2} \cdot \left(\mathbf{z}_{T,k+1} - \mathbf{z}_{T,k} \right) - \frac{2}{\Delta t} \cdot \dot{\mathbf{z}}_{T,k} - \ddot{\mathbf{z}}_{T,k} \tag{27}$$

By substituting(24), (25)and(26) in (23), we obtain now the following equation:

$$\left[\frac{4}{\Delta t^2} \cdot \boldsymbol{M}_{TM} + \boldsymbol{K}_T \right] \cdot \mathbf{z}_{T,k+1} = \mathbf{M}_{TM} \cdot \left(\frac{4}{\Delta t^2} \cdot \mathbf{z}_{T,k} + \frac{2}{\Delta t} \cdot \dot{\mathbf{z}}_{T,k} + \ddot{\mathbf{z}}_{T,k} \right) + \frac{m_U}{\Delta x} \cdot \boldsymbol{\delta} \cdot \ddot{\mathbf{z}}_E \tag{28}$$

With (28), the motion of the entire system $(k \geq 1)$ is calculated recursively using (24), (25)and(26). For this, we specify the initial conditions as follows:

$$\mathbf{z}_T = 0, \ \dot{\mathrm{z}}_\mathrm{T} = 0, \ \ddot{\mathbf{z}}_T = 0 \tag{29}$$

The parameters contained in *Table 1*help to solve the equation (28) under the simplified assumption that we substituted the crossing section by a beam. It consists of 8 rails (8 rails approximately match the mass and bending stiffness of a compact

crossing) of the type UIC60 and displaces by 1.5 mm under a static wheel force of 100 kN (which corresponds to a track stiffness of 66 kN/mm).

Table 1: Parameters of the dynamic model

Parameter	*value*
static wheel force	$F_0 = 100$ kN
unsprung wheel mass	$m_U = 2000$ kg
meter mass	$\bar{m}_T = 480 \times 10^{-3}$ kg/mm
bending stiffness	$EI_T = 2,44 \cdot 10^{10}$ kN·mm²
meter stiffness	$\bar{k}_T = 0,016$ kN/mm²
meter viscosity	$\bar{\eta}_T = 1,67 \cdot 10^{-4}$ kN·s/mm²

2.3 Track geometry error

The track geometry error in the crossing region is composed of a design-related track geometry error and a wear-related track geometry error increasing over time, which is shifted relatively to the former by the offset Δx_{AV} in the main direction of travel. Reference values for the track geometry error provide a special measuring device (*Figure 4*).

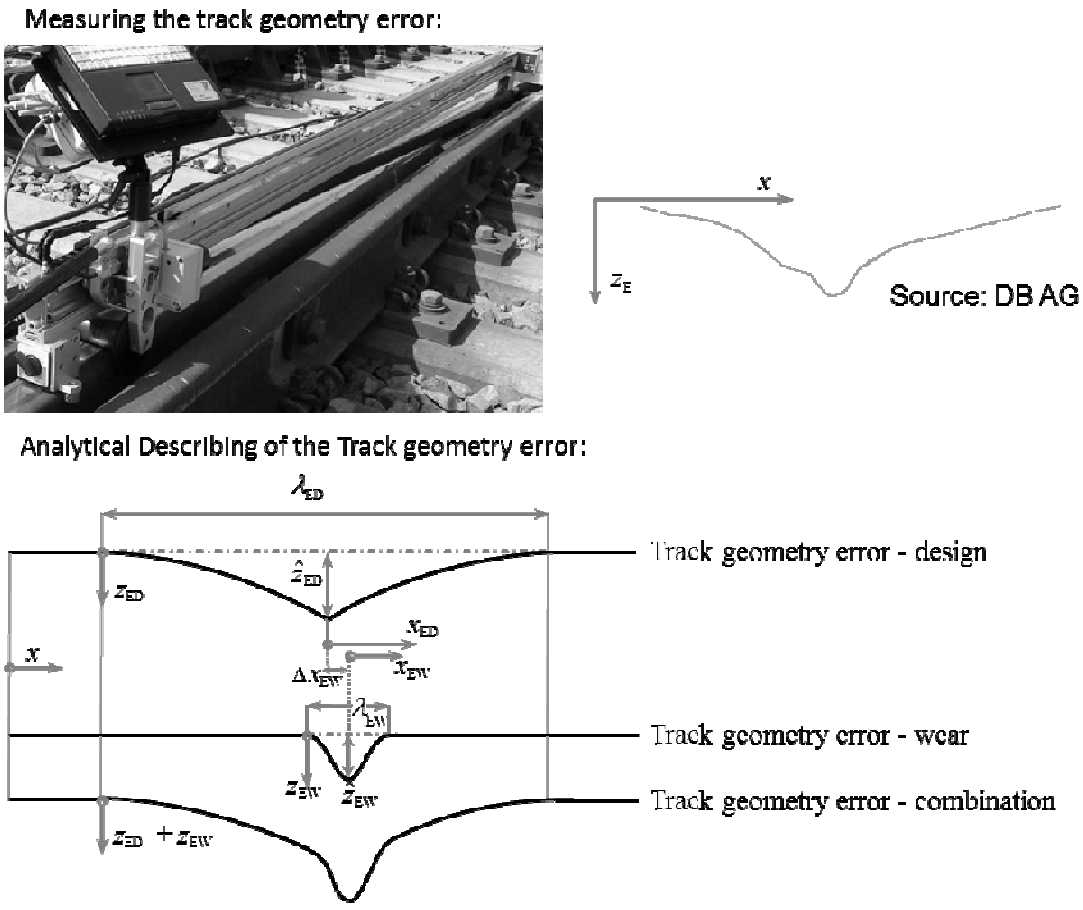

Figure 4:Track geometry error in the crossing region

We replace now the measured track geometry error $\mathbf{z}_E(\boldsymbol{x})$ by an analytical approximation, which is made up of the design-related track geometry error $\mathbf{z}_{ED}(\boldsymbol{x})$ and the track geometry error caused by the wear $\mathbf{z}_{EW}(\boldsymbol{x})$, as *Figure 4* shows:

$$\mathbf{z}_E(\boldsymbol{x}) = \mathbf{z}_{ED}(\boldsymbol{x}) + \mathbf{z}_{EW}(\boldsymbol{x}) \tag{30}$$

The design-related track geometry error is a function of the wavelength λ_{ED} and the wave height $\hat{\mathbf{z}}_{ED}$ (*Figure 4*)

$$\mathbf{z}_{ED} = \frac{4 \cdot \hat{\mathbf{z}}_{ED}}{\lambda_{ED}^2} \cdot \left(\frac{\lambda_{ED}}{2} - \left| \boldsymbol{x} - \boldsymbol{x}_{ED} \right| \right)^2 \text{ for } \left| \boldsymbol{x} - \boldsymbol{x}_{ED} \right| \le \frac{\lambda_{ED}}{2}$$
$$\mathbf{z}_{ED} = 0 \text{ (otherwise)} \tag{31}$$

The wear-related track geometry error is a function of the wavelength λ_{EW} and the wave height $\hat{z}_{\mathrm{EW}}$:

$$\mathbf{z}_{EW} = \frac{\hat{\mathbf{z}}_{EW}}{2} \cdot \left[1 + \cos\left(2\pi \cdot \frac{\left(\boldsymbol{x} - \boldsymbol{x}_{EW} \right)}{\lambda_{EW}} \right) \right] \text{ for } 0 \le \left(\boldsymbol{x} - \boldsymbol{x}_{EW} \right) \le \lambda_{EW}$$
$$\mathbf{z}_{EW} = 0 \text{ (otherwise)} \tag{32}$$

Simplifying, the running in of crossing within first few days of operation will not consider and could be a specific issue for the future investigations. We are assuming that the wave height approximately develops in proportion to the number of load cycles $\boldsymbol{n}$. With the inclusion of the proportionality factor f_{EW}, the following applies:

$$\hat{\mathbf{z}}_{EW} = f_{EW} \cdot \boldsymbol{n} \tag{33}$$

The f_{EW} value was simply calculated by assumption of vertical wear ratio equal 1 mm/year and approx. 1 million load alternations every year (22,5 t axle load and ca. 67,5 kt daily load). Using the parameters contained in *Table 2*, the analytical track geometry error according to (31) and (32) was approximated to the measured track geometry error (*Figure 4, top*).The simulated wheel trajectory on the crossing without wear corresponds well with these parameters for the design irregularity.

Table 2: Parameters of the track geometry error

Parameter	*value*
wave length (design)	$\lambda_{ED} = 2\,\mathrm{m}$
wave height (design)	$\hat{\mathbf{z}}_{ED} = 3\,\mathrm{mm}$
wave length (wear)	$\lambda_{EW} = 0{,}5\ \mathrm{m}$
proportionality factor wave height (wear)	$f_{EW} = 1 \cdot 10^{-6}\ \mathrm{mm}$
offset	$\Delta \boldsymbol{x}_{EW} = 0{,}1\,\mathrm{m}$

wave length (design)	$\lambda_{ED} = 2\,\mathrm{m}$

3. Long-term modelling

Long-time model requires a support-point model to describe the change in the mechanical properties of the underlay. The essential mechanical property of the underlay is the meter stiffness for depiction of the short-term behavior. However, the meter stiffness has a clear dependence on the settling. Thus, a long-term modeling of the meter stiffness is possible only in conjunction with a modeling of the settlement.

The combination of stiffness and settling modeling bases upon on the interpolation point model shown in *Figure 5*. The elastic properties of the under lay express the meter stiffness (excluding hollow position i.e. hollow space between bearer and ballast) and their settling properties in form of two parts. The viscoplastic and viscoelastic parts describes the gravel grain rearrangement and the viscoelastic part describes the fatigue of the gravel angles.

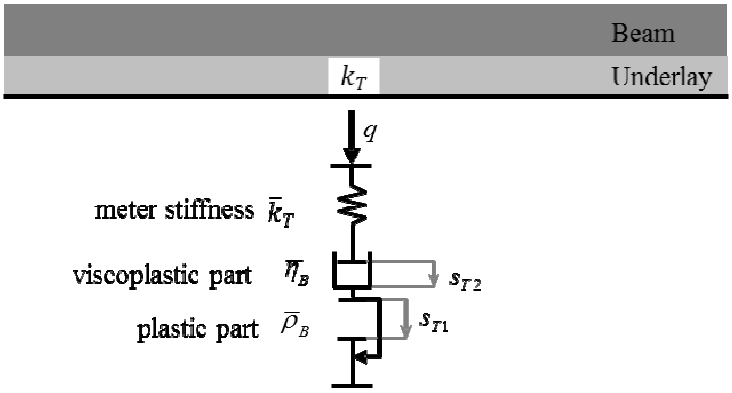

Figure 5: Support-point model of underlay for describing the stiffness and displacement

The analytical implementation of the support-point model shown in *Figure 5* requires two steps:

1. Derivation the underlay meter stiffness of settlement.
2. Derivation the underlay settlement of stress history.

These two steps are covered in the following two sections.

3.1 Underlay meter stiffness derivation of settlement

To differentiate the underlay meter stiffness of the settlement, three basic effects have to be considered:

1. The meter stiffness is composed of the stiffness of bearer, ballast and subsoil. As a first approximation, we assume that only the stiffness and settling of the ballast will increase, while the bearer and subsoil stiffnesses staying preserved. For considering this behavior, the underlay has to be subdivided into vertical elements (bearer, ballast and subsoil).
2. By braking the grain angles with the "long-term", the homogeneous settling and stiffness of the ballast will increase equally.

3. Due to the increased settlement in the crossing area, an additional irregularity appears supplementary to the homogeneous settlement. This depression represents an inhomogeneous settlement. In the middle region of the settling depression, the rail moved more than in its peripheral areas. This increased irregularity corresponds to reduced meter stiffness. Thus, the inhomogeneous settlement and the meter stiffness develop in opposite directions, while according to 2 the homogeneous settlement and the meter stiffness develop in the same direction.

3.1.1 Subdivision of underlay into stiffness elements

The subdivision of underlay into stiffness elements was appropriate carried out to the equivalent diagram *Figure 5*below:

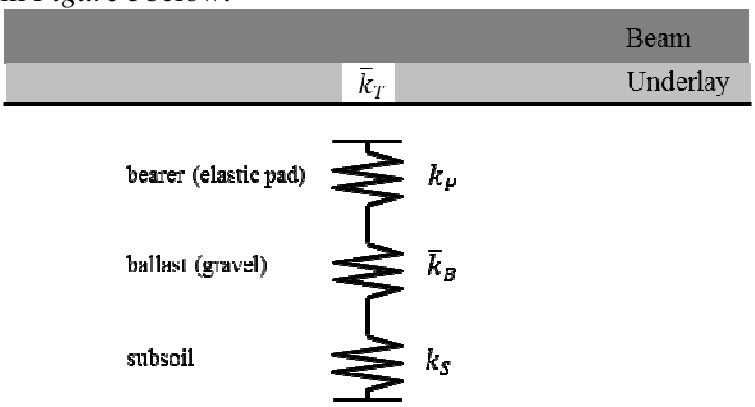

Figure 5: Elastic composition of underlay

The meter stiffness $\bar{k}_T$ of the elastic underlay consists of the series connection of the meter stiffness of subsoil $\bar{k}_S$, ballast (gravel) $\bar{k}_B$ and bearer (elastic pad) $\bar{k}_P$:

$$\bar{c}_T = \frac{1}{\frac{1}{\bar{c}_S} + \frac{1}{\bar{c}_B} + \frac{1}{\bar{c}_P}} \tag{34}$$

To simplify following considerations we assume that settling takes place only within (gravel) ballast. This increases the meter stiffness of the underlay, which, however, cannot be stiffer than the always-effective series connection of the stiffness of the bearer and subsoil:

$$\bar{c}_T \leq \frac{1}{\frac{1}{\bar{c}_P} + \frac{1}{\bar{c}_S}} . \tag{35}$$

3.1.2 Underlay stiffness in dependence with the inhomogeneous settling

The formation of a settlement depression corresponds to the inhomogeneous settling. From a certain expression degree of this settlement depression, an air gap arises in the unloaded state between the track and the ballast upper edge. This clearance closes only under load. The exact provision of this effect requires the transition to non-linear meter stiffness. Nevertheless, in order to be able to keep the assumption of linear meter stiffness, the method was developed below. It has the effect of reducing the meter stiffness over the inner part of the settlement depression (i.e. with concave curvature of the ballast surface) resp. an increase in the meter stiffness over the outer part of the settlement depression (i.e. with a convex curvature of the ballast surface) approximately taken into account.

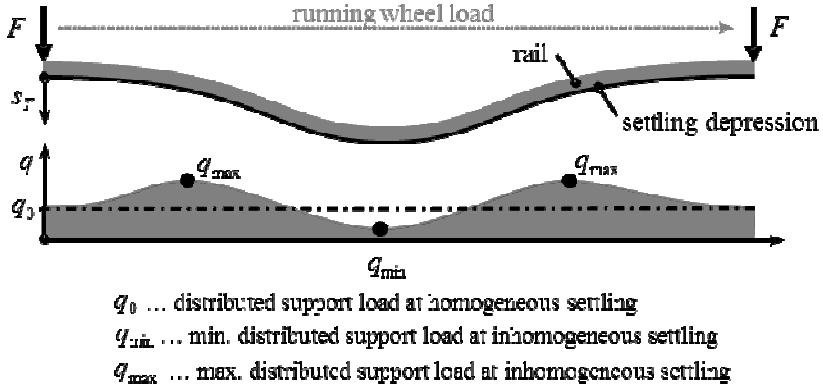

Figure 6: Total distributed support load $q(x)$ by running load F in dependence with the settlement line $s_T(x)$

The distributed support load q (further – support load)describes the underlay meter stiffness. According to *Figure 6,*the size of that load depends on the curvature of the settlement line. With concave settlement line curvature (in the middle area of the settlement depression), the induced distributed support load is smaller than in the undisturbed track area. In the case of convex settlement line curvature (on both sides of the settlement depression), the induced support load is greater than in the undisturbed track area.

The development of the meter stiffness is affine to the depicted development of the support load. Therefore, the meter stiffness dependence on the inhomogeneous settling describes analogously the relation (35).

$$\bar{k}_T(x) = \left(1 - \frac{s_T''(x)}{s_{T0}''}\right) \cdot \bar{k}_{T0} \tag{36}$$

The settlement line curvature s_T'', the limit value of it s_{T0}'' and the original meter stiffness $\bar{k}_{T0}$ (i.e. the meter stiffness without settlement line curvature) identify the effective meter stiffness $\bar{k}_T$. If the settlement line curvature takes value zero, then the meter stiffness equals the original meter stiffness. For positive settlement line curvatures (concave ones), the meter stiffness is smaller than the original meter stiffness. For negative settlement line curvatures (convex ones), the meter stiffness is greater than the original. The threshold value of curvature corresponds to the maximum possible

concave curvature of the beam. If the settlement line curvature reaches this curvature limit, then the meter stiffness becomes zero.

3.1.3 Underlay stiffness in dependence with the homogeneous settling

As already mentioned, we assume that the entire settlement occurs within (gravel) ballast. Depending on this settlement, the meter ballast stiffness $\overline{k}_B$ increases or decreases the ballast resilience $1/\overline{k}_B$. The experiments (*Figure 8*) evidence that the ballast settlement runs toward a specific limit value s_{T0}. It is based on the simplistic assumption that the ballast resilience is proportional to settlement s_T up to that limit. The ballast in its new condition has the settlement of zero and the stiffness value $\overline{k}_{B0}$. When settlement reaches its limit s_{T0}, the ballast layer resilience is exhausted ($1/\overline{k}_B = 0$) resp. its stiffness becomes infinite ($\overline{k}_B \to \infty$). Thus:

$$\overline{k}_B(x) = \frac{\overline{k}_{B0}}{\left(1 - \frac{s_T(x)}{s_{T0}}\right)}. \tag{37}$$

3.1.4 Total stiffness of the underlay

By inserting (36)and(37) in(34), the meter underlay stiffness is obtained as a function of the homogeneous $s_T(x)$ and inhomogeneous $s_T''(x)$ settlement:

$$\overline{k}_T(x) = \frac{\left(1 - \frac{s_T''(x)}{s_{T0}''}\right)}{\frac{1}{\overline{k}_S} + \frac{\left(1 - \frac{s_T(x)}{s_{T0}}\right)}{\overline{k}_{B0}} + \frac{1}{\overline{k}_P}} \tag{38}$$

The next assumption for the new underlay condition is that the stiffnesses of the bearer, ballast and subsoil are distributed in approximately equal proportions. In this case, (38) was simplified to:

$$\overline{k}_T(x) = \frac{\left(1 - \frac{s_T''(x)}{s_{T0}''}\right)}{2 + \left(1 - \frac{s_T(x)}{s_{T0}}\right)} \cdot \overline{k}_{B0} \tag{39}$$

Formula (39) calculates the meter underlay stiffness $\overline{k}_T(x)$ in accordance with the meter ballast stiffness in its new condition $\overline{k}_{B0}$, the homogeneous settlement $s_T(x)$ with

its settling limit $s_{T0}(x)$ and the inhomogeneous settlement line curvature $s''_T(x)$ with its limit $s''_{T0}(x)$. *Figure 7*shows the behavior of (39).

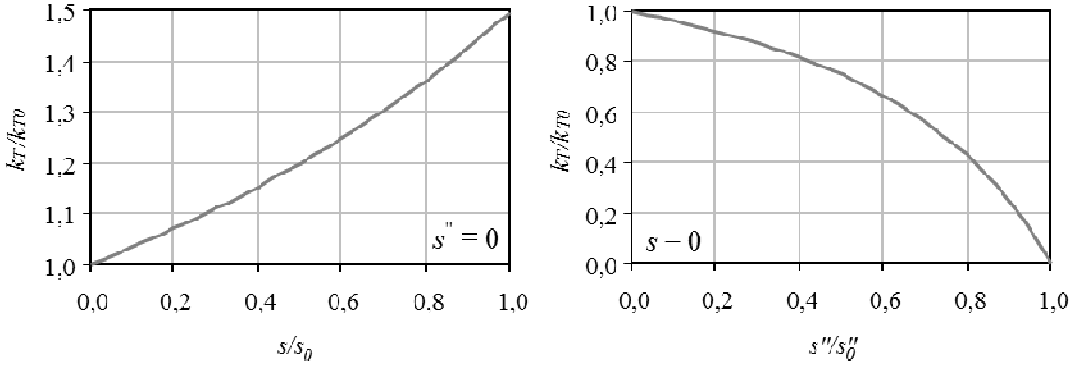

Figure7: Influence of homogeneous settlement (left) and inhomogeneous settlement (right) on the meter stiffness

Figure 7 shows the ambivalent effect of the settlement depression (its middle region) below the crossing nose. On the one hand, the increased homogeneous settling produces increased meter stiffness (*Figure 7*, right), on the other hand, the concave curvature produces a reduced meter stiffness (*Figure 7*, left). This mutual compensation suggests a comparatively small change in meter stiffness below the crossing nose.
Using the parameters collected in*Table 3*the meter stiffness results according to (39).

Table 3: Parameters of settlement-dependent meter stiffness

Parameter	*value*
meter stiffness of (gravel) ballast	$\overline{k}_{B0} = 0,012$ kN/mm²
limit settlement	$s_{T0} = 15$ mm
limit curvature	$s''_{T0} = 2 \cdot 10^{-6}$ mm

3.2 Underlay settlement derivation of the load history

The settlement behavior of the ballast is known from many experimental measurements (Gerberand Fengler, 2010) and observations (Lichtberger,2003). However, the measurement results are quite different, that effects in difficulty of interpretation. To make clear the qualitative and quantitative behavior of railway ballast, the experimental measurements of TU Dresden were carried out. The experimental setup is shown at *Figure 8*.

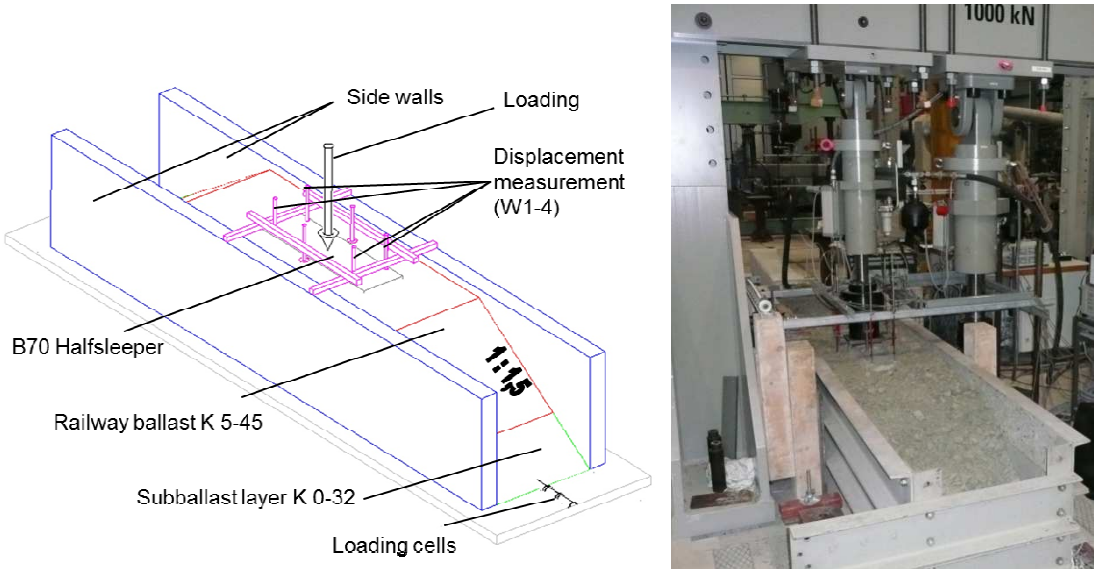

Figure 8: The experimental measurements of ballast settlements (TU Dresden)

The sleeper settlements and ballast pressure on the subgrade were measured in the experiment. The cyclic loading (counted in load cycles) was simulated with a hydropulse device. The loading corresponded to the equivalent wheel force of 100 kN at a frequency of 18 Hz (this agrees to a axles distance of 3 m and a speed of 200 km/h). The ballast layer was built over the subballast layer. Both layers were completely compacted. The settlement measurement results as well as the curve approximation are shown at *Figure 9(left).*

The similar settlement behavior is confirmed by in-situ observations [4]. *Figure 9*shows the results of track settlement for unconsolidated ballast (wheel force $\boldsymbol{F}$).

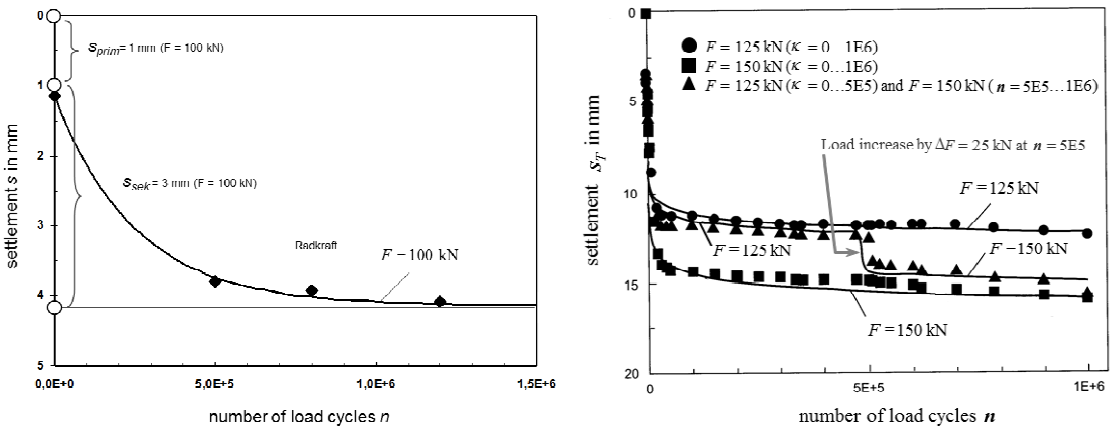

Figure 9: Settlement behavior of ballast:
left –experimental results of TU Dresden,
right – in-situ observations(Lichtberger., 2003)

From the experimental results of a ballast test in *Figure 9*, it becomes clear that the settling behavior of the ballast has to be described as the sum of an almost time-independent primary part and its time-dependent secondary part. As soon as the ballast is under the static load (wheel force), it responds with an immediate, in the first

approximation time-independent primary settlement. The cyclic reloading induces a further secondary settlement, which increases with the number of load cycles. Of particular interest is the settlement behavior in accordance with *Figure 9*, if after half a million load changes the static wheel force is increased by 25 kN. In this case, the ballast reacts immediately with a further primary settling. It follows from that behavior that the primary settling depends on the static wheel force and the secondary settling on the load cycle number.

Correspondent to *Figure 5*, the time-independent behavior (plastic part s_{T1} = primary settling) associatively described as a friction member and the time-dependent behavior (viscoplastic part s_{T2} = secondary settling) associatively as a viscous damper. The total composition results from summation of the plastic and viscoplastic settling fraction:

$$s_T = s_{T1} + s_{T2} \tag{40}$$

3.2.1 Plastic settlement of underlay

The plastic settlement s_{G1} occurs immediately as shown in *Figure 9*, if the induced support load q_0 is greater than the maximum support load $(q_0)_{\max}$ previously encountered in the load history. This behavior has a physical interpretation. The increase in the maximum support load leads to a rearrangement of the ballast structure. The relationship between plastic settlement and load (wheel force or support-point load) is approximately linear. With the plastic constants c_{P1} follows:

$$s_{T1} = c_{P1} \cdot (q_0)_{\max} \tag{41}$$

3.2.2 Viscoplastic settlement of underlay

In respect of *Figure 9*, the settlement behavior also depends on the number of load cycles. This behavior also has a physical meaning. The contacting ballast angles are subjected to alternating stress and breakage. The fatigue is noticeable by breaking the grain angles off after a certain number of load cycles. However, this process tends to a stable state, since the contact stress between the gravel grains after their damage is so small that no subsequent fatigue takes place. The next step is to choose an exponential approach with the viscoplastic constants c_{P2} for describing that decay behavior of the viscoplastic settlement s_{T2}. In addition, considering the fact that the fatigue increases with the load, we formulate the viscoplastic settling in linear relation with the plasticity. Thus:

$$s_{T2} = \frac{1}{3} \cdot s_{T1} \cdot \left(1 - e^{c_{P2} \cdot c}\right) \tag{42}$$

3.2.3 Total settlement of underlay

The total settlement is achieved by inserting (41) and (42)in (40):

$$s_T = c_{P1} \cdot (q_0)_{\max} \cdot \left[1 + \frac{1}{3} \cdot \left(1 - e^{c_{P2} \cdot c} \right) \right] \tag{43}$$

Using the parameters in *Table 4* to calculate the total settlement in accordance with (43) it is necessary to bring it into conformity with the experimentally defined settlement behavior respectively *Figure 9.*

Table 4: Parameters of settlement

Parameter	*value*
plastic constant	$c_{P1} = 0{,}16\,\text{mm²/N}$
viscoplastic constant	$c_{P2} = -3 \cdot 10^{-6}$

3.3 Algorithm for coupling settlement and stiffness

The short-term and the long-term behavior are coupled with each other. For short-term behavior, the underlay stiffness is essential. As the underlay resilience increases, the dynamic forces also increase. The increased dynamic forces in turn induce an increased settling and thus influence the long-term behavior. This coupling of settling and stiffness is applied consecutively in form of an algorithm on the entire beam.

The n-th overrun of the wheel force above the beam (rail) induces a support load $q_{0,c}(x_p, t)$ in a point x_p under the beam. This load results from the meter stiffness $\bar{k}_{T,c}(x_p)$ and the meter viscosity $\bar{\eta}_{T,c}(x_P)$ as a function of the beam displacement $\mathbf{z}(\mathbf{x_p}, \mathbf{t})$ and velocity of that movement $\dot{\mathbf{z}}(\mathbf{x_p}, \mathbf{t})$. In matrix notation, the vector of the induced support load $\mathbf{q_{0,c}}$ depends on the vector of the meter stiffness $\bar{k}_{T,c}$, the displacement vector $\mathbf{z}_{n,c}$ (movement of each beam element) and the vector of the velocity $\dot{\mathbf{z}}_{n,c}$:

$$\mathbf{q_{0,c}} = \boldsymbol{MAX}_N (\bar{k}_{T,c} \cdot \mathbf{z}_{n,c} + \bar{\eta}_G \cdot \dot{\mathbf{z}}_{n,c}) \tag{44}$$

The vector of induced support load $\mathbf{q_{0,c}}$ results in a plastic settlement (41) if the current induced support load is greater than the previous history of load history. For the vector of plastic settlement $\mathbf{s}_{T1,c}$, equality becomes:

$$\mathbf{s}_{T1,c} = \begin{vmatrix} c_{P1} \cdot q_{0,j,c-1} \text{ für } \left(c_{P1} \cdot q_{0,j,c} \right) < \left(c_{P1} \cdot q_{0,j,c-1} \right) \\ c_{P1} \cdot q_{0,j,c} \text{ für } \left(c_{P1} \cdot q_{0,j,c} \right) \geq \left(c_{P1} \cdot q_{0,j,c-1} \right) \end{vmatrix} \tag{45}$$

Therefore, the vector of the plastic settlement $\mathbf{s}_{T1,c}$ provides the next calculation of the vector of the viscoplastic settlement $\mathbf{s}_{T2,c}$ like the formula (42) shows:

$$\mathbf{s}_{T2,c} = \frac{1}{3} \cdot \left(1 - e^{c_{P2} \cdot c}\right) \cdot \mathbf{s}_{T1,c} \tag{46}$$

Hence, the total settlement in form of vector $\mathbf{s}_{T,c}$ results from (40):

$$\mathbf{s}_{T,c} = \mathbf{s}_{T1,c} + \mathbf{s}_{T2,c} \tag{47}$$

The inhomogeneous settlement vector $\mathbf{s}''_{T,c}$ can be derived directly from the homogeneous settlement vector $\mathbf{s}_{T,c}$ (total settlement). Here are the initial conditions:

$$\mathbf{s}_{T,c=0} = \mathbf{0}\,,\ \mathbf{s}''_{T,c=0} = \mathbf{0} \tag{48}$$

As soon as the settlement after the c -th overrun is known, it can be used to define the meter stiffness at the $(c+1)$-th overrun using (39):

$$\overline{k}_{T,c+1} = \frac{\left(1 - \frac{\mathbf{s}''_{T,c}}{\mathbf{s}''_{T,1}}\right)}{2 + \left(1 - \frac{\mathbf{s}_{T,c}}{s_{T0}}\right)} \cdot \overline{k}_{B0} \tag{49}$$

The start conditions are:

$$\overline{k}_{T,c=0} = \frac{\overline{k}_{B0}}{3} \tag{50}$$

With the meter stiffness $\overline{k}_{T,c+1}$ and the help of (49) for the cycle $c+1$, the dynamic model provides the maximum displacement $\mathbf{z}_{\max,c+1}$. By means of the relations (44) - (49)it follows the meter stiffness $\overline{k}_{T,c+2}$, etc.

4. Numerical results and measurements

The numerical simulation was carried out based on the developed model of short- and long-term dynamic behavior. The long-term deformation in crossing section consists of two basic effects:

1. The growth of the track geometry error. *Figure 10*showsthe development of the crossing point wear corresponding well with load cycle number n [1].In this case, one recognises that the displacement of the crossing point wear is in the main direction of movement. This offset results from the phase shift between the excitation (track geometry error) and the response (wheel - rail contact force) of the vibration system wheel - rail.

[1] With an average track line load, 3000 - 1 million - 2 million load changes correspond to a service life of 1 day - 1 year - 2 years.

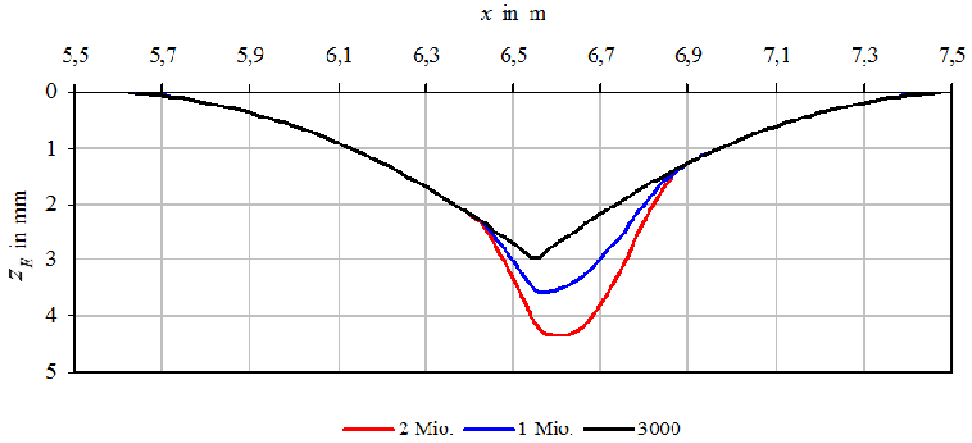

Figure 10: Track geometry error in crossing area in dependence with the load cycle number ***n***

2. The growth of settlement and the change in the ballast meter stiffness. The wheel trajectory due to settlement developing with the load cycles number shows *Figure 11*, whereby the position of the constructive track geometry error (TGE - design) is also implied here for better orientation. The shift of the settlement wave with respect to the constructive TGE in the direction of train motion.

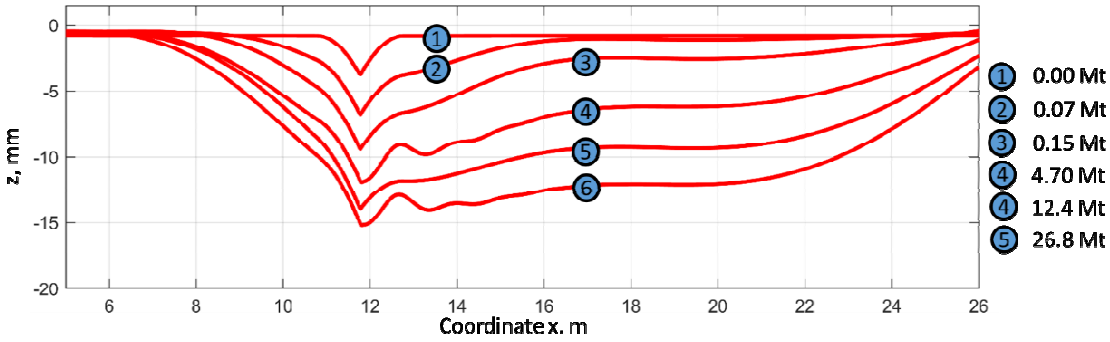

Figure 11: Settlement in crossing section in dependence with the load cycle number ***n***

The experimental measurement of settlement in crossing section is performed with vehicle based measurements diagnostic system ESAH-F. The measured accelerations in axle-box after double integration provide the wheel trajectories while common crossing passing. The common crossing was measured 5 times during its overall lifecycle up to 27,2 Mt (*Fig.12*).

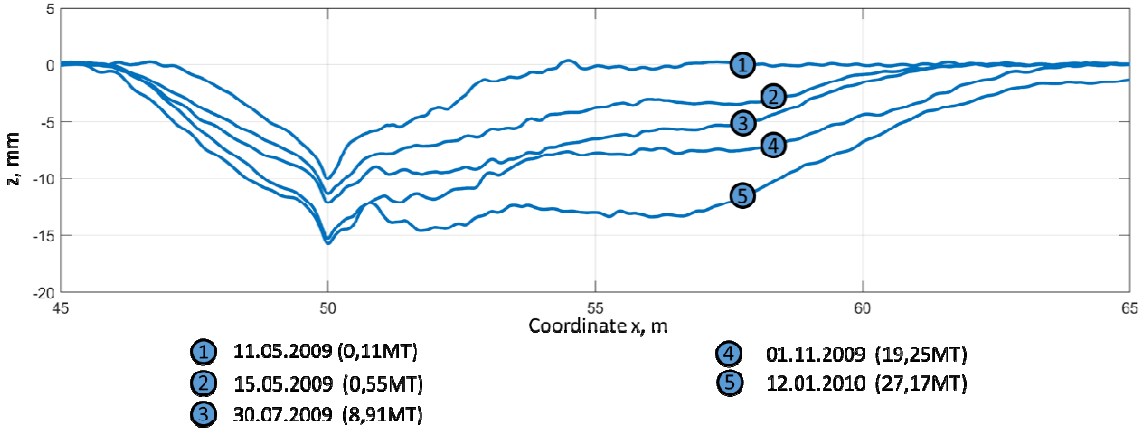

Figure 12: The vehicle based measurements of common-crossing settlements with diagnostic system ESAH-F during its lifecycle
Source: DB Systemtechnik

The comparison of the simulated and measured results shows relatively gut similarity. Both results demonstrate comparatively quick inhomogeneous settlements for the period of the first 10 thousand axles (0.15Mt) that can reach up to 2/3 of the settlements during the overall crossing lifecycle. The initial inhomogeneous settlements occur mostly under the frog nose of common crossing. The secondary settlements are most intensive in track zone up to 10 m after the common crossing. The settlement wave grows also in the direction against the train motion beginning on the point of crossing and up to 5 m before.

The comparison to the results of other researchers shows many similarities but although differences. The theoretical results of Xin et al.(2014) and the experimental measurements in turnouts of Plášek & Hruzíková(2017) are considered for the comparison. The particularity of the both theoretical and experimental studies is that they cannot be directly compared. The settlements of the common crossing as well as of the ordinary tack are intensive at the beginning and slow rapidly down after about 1 Mt of traffic. The theoretical study of Xin et al.(2014) present the initial settlements and the experimental investigations of Plášek & Hruzíková (2017) take into account the settlements after some stabilization of track. Therefore, the comparison is carried out for 2 lifecycle phases: initial and overall. The results are shown in Table 5.The results correspond well enough to the present study, taking into account different operational conditions for both compared studies.

Table 5: Comparison of results

Parameter	Theoretical study by Xin et al.(2014)	Present study, theory/measurements	Experimental study by Plášek & Hruzíková (2017)
overall intensity of settlements, mm/10Mt	-	4.5/4.6	3.39
Initial intensity of settlements, mm/1 Mt	4.8	5.5/7.8	-

5. Summary and subsequent studies

The results of numerical simulation and vehicle based measurements of long-term ballast settlements under the common crossing are presented in the paper. The model takes into account the main factors that influence the long-term settlements behavior of railway ballast: the dynamic loading, track stiffness and inhomogeneous longitudinal ballast stiffness due to sleeper voids, viscoplastic properties of ballast settlements. This approach allows us to reach relatively good numerical agreement of measured settlements. The settlements behavior of railway ballast under the common crossing is ambiguous and can be divided in two phases: initial deep settlement and secondary wide ones. On the one side the quick initial settlement, appears due to plasticity properties of ballast layer, on the other – due to big dynamic loading in frog zone. The quick deceleration of settlements is connected with the development of sleeper voids and reduction of track stiffness. This, in turn, results in reduction of dynamic loading in the frog section, but at the same time, it causes the overloading of the side zones. That effect initiates the growth of settlement wave length without significant growth in depth.

The developed model can be used for switch maintenance as well as switch structure optimization with the aim to slow down the settlement intensity. The first settlement phase is inevitable only with maintenance works without the change of switch structure. Therefore, the main optimization outcome could be reached with slowing down the settlement in the secondary phase. Moreover, the reduction of dynamic loading due to the decrease of track stiffness and initial settlement wave can have the positive influence on frog nose lifecycle. The study of the effects could be the aim of the future research.

References

Augustin, S., Gudehus, G., Huber, G., Schühneman, A. (2003) “Numerical model and laboratory tests on settlements of ballast track”, In: Popp, K. (eds) *System dynamics and long-term behavior of railway vehicles*, Berlin Heidelberg: Springer-Verlag. 488pp.DOI: 10.1007/978-3-540-45476-2

Esveld, C. (2001). Modern railway track (Vol. 385). Zaltbommel, The Netherlands: MRT-productions.

Fischer, S. (2017)“Breakage Test of Railway Ballast Materials with New Laboratory Method”. *Periodica Polytechnica Civil Engineering,* 61 (4), pp. 794-802. doi.org/10.3311/PPci.8549

Gerber, U. Fengler, W. (2010)Setzungsverhaltendes Schotters. *Eisenbahntechnische Rundschau*, 4, pp. 170-175.

Gerber, U., Zoll, A., Fengler, W. (2013) “Fahrzeugbasierte Beurteilung des Herzstückverschleißes” [Vehicle-based assessment of wear on common crossings],*EI-Eisenbahningenieur*(5), pp. 26-30.

Gerber, U., Zoll, A., Fengler, W. (2015) “Verschleiß und Fahrflächenermüdung an Weichen mit starrer Herzstückspitze” [Wear and Rolling Contact Fatigue on common crossings of railway turnouts]. *ETR – Eisenbahntechnische Rundschau*, 1, pp. 36-41.

Holtzendorff, K. (2003) Untersuchung des Setzungsverhaltens von Bahnschotter und der Hohllagenentwicklung auf Schotterfahrbahnen. *Ph.D. thesis*, Technische Universität Berlin. 130pp.

Izvolt, L., Harusinec, J., Smalo, M. (2018) Optimisation of transition areas between ballastless track and ballastedtrack in the area of the tunnel turecky vrch. *COMMUNICATIONS Scientific Letters of the University of Zilina,*20(3), pp. 67-76.

Izvolt, L., Kardos, J. (2011)"Influence of Parameters of Railway Track Construction on Vertical Dynamic Interaction VehicleTrack".*COMMUNICATIONS Scientific Letters of the University of Zilina*, 3, pp. 63-70.

Kovalchuk, V., Kovalchuk, Y., Sysyn, M., Stankevych, V., Petrenko, O. (2018a)"Estimation of carrying capacity of metallic corrugated structures of the type multiplate mp 150 during interaction with backfill soil". *Eastern-European Journal of Enterprise Technologies*, 1/1 (91), pp.18-26.doi.org/10.15587/1729-4061.2018.123002

Kovalchuk, V., Sysyn, M., Hnativ, Y., Bal, O., Parneta, B., Pentsak, A.(2018b)"Development of a promising system for diagnosing the frogs of railroad switches using the transverse profile measurement method". *Eastern-European Journal of Enterprise Technologies*, 2(1-92), pp. 33-42. DOI: 10.15587/1729-4061.2018.125699

Kovalchuk, V., Sysyn, M.,Sobolevska, J., Nabochenko, O., Parneta, B., Pentsak, A. (2018c) "Theoretical study into efficiency of the improved longitudinal profile of frogs at railroad switches". *Eastern-European Journal of Enterprise Technologies*, 4(1-94), pp. 27-36. DOI: 10.15587/1729-4061.2018.139502

Lichtberger, B. (2003). Handbuch Gleis: Unterbau, Oberbau, Instandhaltung, Wirtschaftlichkeit. Hamburg: Tetzlaff Verlag, pp.43-46.

Nabochenko, O., Sysyn, M., Kovalchuk, V., Kovalchuk, Yu., Pentsak, A., Braichenko, S. (2019) "Studying the railroad track geometry impairment as a result of an uneven subsidence of the ballast layer". *Eastern-European Journal of Enterprise Technologies*, 7. doi: 10.15587/1729-4061.2019.154864

Nagy, R. (2017) "Description of rail track geometry deterioration process in hungarian rail lines no. 1 and no. 140". *Pollack periodica* (12), 3, pp. 141–156.

Németh, A., Fischer, S.(2018) "Investigation of glued insulated rail joints with special fiber-glass reinforced synthetic fishplates using in continuously welded tracks". *Pollack Periodica*, 13(2), pp. 77-86. DOI: 10.1556/606.2018.13.2.8

Plášek, O., Hruzíková, M., Svoboda, R., Vendel, J. (2015)"Influence of under sleeper pads on track quality".*Akustika*, 23(1), pp. 28-33.

Plášek, O., Hruzíková, M.(2017) "Under sleeper pads in switches& crossings". IOP Conference Series: Materials Science and Engineering, 236(1),012045. doi:10.1088/1757-899X/236/1/012045

Popp, K., Knothe, K., Pöpper, K. (2005) System dynamics and long-term behaviour of railway vehicles, track and subgrade: report on the DFG Priority Programme in Germany and subsequent research, *Vehicle System Dynamics*, 43:6-7, pp. 485-521. DOI: 10.1080/00423110500143728

Sysyn, M., Gerber, U., Kovalchuk, V., Nabochenko, O.(2018) "The complex phenomenological model for prediction of inhomogeneous deformations of railway ballast layer after tamping works". *Archives of Transport,* 46(3), pp. 91-107. DOI: 10.5604/01.3001.0012.6512

Sysyn, M., Kovalchuk, V., Jiang, D. (2018) "Performance study of the inertial monitoring method for railway turnouts". *International Journal of Rail Transportation*, 4 (4). doi.org/10.1080/23248378.2018.1514282

Sysyn, M., Gruen, D., Gerber, U., Nabochenko, O., Kovalchuk, V. (2019a) "Turnout monitoring with vehicle based inertial measurements of operational trains: a machine learning approach". *COMMUNICATIONS Scientific Letters of the University of Zilina*, 20(4), pp. 21-27.

Sysyn, M., Nabochenko, O., Gerber, U., Kovalchuk,V. (2019b) "Evaluation of railway ballast layer consolidation after maintenance works". *Acta Polytechnica*, 58(6), pp. 1–16.

Uhl, T., Mendrok, K., Chudzikiewicz, A. (2010)"Rail track and rail vehicle intelligent monitoring system". *Archives of Transport*, 22(4), pp. 496-510. DOI: 10.2478/v10174-010-0030-1

Wang, H., Markine, V. (2018) "Modelling of the long-term behaviour of transition zones: prediction of track settlement". *Engineering Structures*, 156, pp. 294-304.https://doi.org/10.1016/j.engstruct.2017.11.038

Zoll, A., Gerber, U., Fengler, W. (2016) "Das Messsystem ESAH-M" [The measuring system ESAH-M].*EI-Eisenbahningenieur Kalender*, (2016), pp. 49-62.

Xin, Li, Jens, C.O., Nielsen & Björn, A., Pålsson (2014) "Simulation of track settlement in railway turnouts". *Vehicle System Dynamics*, 52, sup1, pp. 421-439. DOI:10.1080/00423114.2014.904905

Acknowledgements

We owe our greatest debt of gratitude to Germany Railway Company (DB Systemtechnik GmbH) and WITT Elektronik GmbH for their financial support and experimental data.